Composites: Part A 199 (2025) 109205

Contents lists available at ScienceDirect

Composites Part A

journal homepage: www.elsevier.com/locate/compositesa

A conductive composite hydrogel for promoting bone defect regeneration through microcurrent stimulation

Qiangwang Geng [a,1], Huichao Fu [b,1], Xiongjie Liang [b], Xiaoyan Wang [b], Yunjiao Wu [c], Fenghua Zhang [a,*], Gongping Xu [b,*], Jinsong Leng [a,*]

[a] Centre for Composite Materials and Structures, Harbin Institute of Technology (HIT), Harbin 150080, China
[b] Department of Orthopedic Surgery, The Second Affiliated Hospital, Harbin Medical University, No. 246 Xuefu Road, Harbin 150086, China
[c] Department of Respiratory Medical Oncology, Harbin Medical University Cancer Hospital, Heilongjiang, Harbin 150081, China

ARTICLE INFO

Keywords:
Conductive hydrogel
Composite hydrogel
Biocompatible
Bone Repair

ABSTRACT

Although microcurrent stimulation (MCS) has been demonstrated to enhance tissue repair, a significant limitation of MCS in clinical applications is the scarcity of suitable biomaterials, which can effectively deliver microcurrents while conforming well to bone tissue. In this study, carbon nanotubes (CNTs) and graphene oxide (GO) were incorporated into double-network hydrogels synthesized from gelatin and polyacrylamide (PAAm) to render the hydrogels conductive. CNTs were identified as the optimal nanofillers via simulations and experimental investigations. The optimal gelation and mechanical properties of the hydrogel are achieved when the initiator content is 0.8 wt%. The obtained conductive hydrogel exhibits mechanical properties of 0.23 MPa, meeting the biomechanical requirements. When both CNT and GO are added at 1.0 wt%, the conductivity of the CNT-included composite hydrogel is 10.17 times that of the GO-included hydrogel. Meanwhile, this CNT-doped composite hydrogel demonstrates excellent biocompatibility. Upon implantation of the hydrogel into an animal model with skull defects followed by electrical stimulation, it was confirmed that these hydrogels can promote skull repair. This conductive hydrogel holds promise in addressing current challenges related to material acquisition difficulties and postoperative infection risks associated with bone repair procedures.

1. Introduction

Bone defects represent one of the most prevalent orthopedic conditions, primarily resulting from trauma, tumor resection, infection, or congenital disorders [1–3]. The principal treatments currently employed include autografts, allografts, and synthetic bone substitutes [4]. However, these approaches are not without challenges; notably, synthetic bone substitutes often exhibit a lack of biological activity and osteoinductive properties, significantly limiting their effectiveness in facilitating complete bone regeneration [5–7]. Considering these limitations, the exploration of innovative strategies to address bone defects has become increasingly critical.

Bioelectrical signals, as a biophysical stimulus, are prevalent in the microenvironment of natural bone tissue and play an important role in promoting the healing process of bone defects [8–10]. There is increasing evidence that exogenous electrical stimulation can modulate bioelectrical signals and accelerate the healing of bone defects. Exogenous electrical stimulation therapies approved by the U.S. Food and Drug Administration have demonstrated their ability to accelerate the healing of bone defects [11], Calcium ions (Ca^{2+}) are a key second messenger for intracellular signaling. Increasing evidence highlights the calcium signaling pathway in osteogenic differentiation [12,13]. As a result of electrical stimulation, cell membrane depolarization leads to the opening of calcium channels, which increases Ca^{2+} influx [14], and as a second messenger, Ca^{2+} activates the PI3K/AKT, MAPK, and Wnt/-βcatenin signal pathway, which in turn regulates subsequent osteogenesis-related genes and promotes osteogenic differentiation of bone marrow mesenchymal stem cells.

Recent advancements in biomaterials and biophysical stimulation techniques have unveiled new possibilities for treatment of bone defects [15–17]. Among these innovations, the application of MCS in conjunction with conductive biomaterials has demonstrated considerable

* Corresponding authors.
E-mail addresses: fhzhang_hit@163.com (F. Zhang), 13704846805@163.com (G. Xu), lengjs@hit.edu.cn (J. Leng).
[1] These authors contributed equally as the first author.

https://doi.org/10.1016/j.compositesa.2025.109205
Received 9 June 2025; Received in revised form 19 July 2025; Accepted 22 July 2025
Available online 26 July 2025

promise [18]. These emerging methodologies aim to mitigate the shortcomings associated with traditional treatments while promoting functional and durable bone repair [19]. MCS is a form of tissue regeneration that influences cell migration, proliferation, and differentiation through the application of low electric currents to enhance tissue repair [20]. This technique shows significant potential in bone regeneration, as microcurrent stimulation (MCS) has been demonstrated to enhance osteogenic differentiation by upregulating critical markers such as alkaline phosphatase (ALP), osteocalcin, and type I collagen. MCS achieves this by activating essential intracellular signaling pathways, including the mitogen-activated protein kinase (MAPK) and Wnt/β-catenin pathways [21–24]. For instance, Konstantinou et al. demonstrated that microcurrents stimulate cell proliferation and migration via pathways involving ERK 1/2 or p38-dependent manner. Additionally, microcurrents induce fibroblasts and osteoblast-like cells to secrete transforming growth factor-beta-1 (TGF-β1). Transcriptomic analysis further revealed that microcurrent exposure enhances the transcriptional activation of genes associated with the Hedgehog, TGF-β1, and MAPK signaling pathways—processes that are crucial for osteoblast differentiation and bone mineralization [25]. In addition, MCS facilitates angiogenesis through the induction of pro-angiogenic factor secretion, most notably vascular endothelial growth factor (VEGF), which is vital for successful bone regeneration [26–28]. However, a significant limitation of MCS in clinical applications is the absence of suitable biomaterials capable of seamlessly integrating with bone tissue while efficiently delivering microcurrents.

To address the limitations of traditional bone repair methods, research on conductive hydrogels has emerged as a key focus, particularly in combination with microcurrent stimulation (MCS) technology. Due to their high-water content and excellent biocompatibility, hydrogels are widely used in tissue engineering [29–31]. Incorporating conductivity into hydrogels further expands their applications, especially in electrically sensitive tissues such as bone. Conductive hydrogels are typically synthesized by integrating conductive components—such as polyaniline (PANI) and polypyrrole (PPy)—or conductive fillers like carbon nanotubes and graphene into the hydrogel matrix [32–35]. While this approach enables hydrogels to transmit electrical signals, it often compromises their biocompatibility, thereby limiting their applications (Table S1).

Gelatin, a natural biopolymer sourced from collagen, is widely recognized for its biocompatibility, biodegradability, and versatile properties [36–38]. As an affordable and sustainable material, it demonstrates strong gelation, film-forming ability, and emulsification, making it valuable in food science, pharmaceuticals, and tissue engineering. Its non-toxic nature, adjustable mechanical strength, and thermal stability enable tailored modifications for diverse industrial applications. Moreover, gelatin supports cell adhesion and proliferation [39,40]. However, studies on conductive gelatin-based hydrogels remain scarce.

In this study, we developed a conductive hydrogel exhibiting excellent biocompatibility. High-strength double-network hydrogels can be obtained by introducing acrylamide chain segments into gelatin to form a double-network (DN) hydrogel. This strategy enhances the mechanical properties of the hydrogel while maintaining its biocompatibility and degradability. Through a comparative analysis of simulation and experimental results, CNTs were selected over GO due to their superior conductivity. The synthesis of gelatin/polyacrylamide/CNTs(G-A-CNTs) hydrogels involved a systematic investigation into the effects of thermal initiators on hydrogel properties, utilizing ab initio quantum chemical calculations alongside experimental validation to identify the optimal initiator concentration [41]. The resulting conductive hydrogel demonstrated remarkable stability in conductivity as well as biocompatibility. *In vivo* implantation studies in mice with skull defects revealed that the hydrogel was capable of fully repairing these defects; specifically, the G-A-CNTs hydrogel containing 0.75 % CNTs achieved complete repair when combined with microcurrent stimulation. This study introduces an innovative approach for employing conductive hydrogels in cranial repair applications.

2. Materials and methods

2.1. Materials

Acrylamide (AAm, 99 %), gelatin, and N,N'-methylenebis-acrylamide (MBA) were sourced from Aladdin (Shanghai) Co., Ltd. Potassium persulfate (KPS) was obtained from Sinopharm Chemical Reagent Co., Ltd. Multi-walled carbon nanotubes were acquired from Suzhou Tanfeng Technology Co., Ltd., while single-layer graphene was procured from Shenzhen Suiheng Graphene Technology Co., Ltd.

2.2. Fabrication of Gelatin/PAAm/CNTs hydrogel

Gelatin/acrylamide/carbon nanotube or gelatin/acrylamide/graphene hydrogel is synthesized by the following steps: first, add 15 wt% gelatin, 25 wt% AAm, and 0.05 wt% MBA crosslinker to the beaker, then add deionized water(10 g), heat it to 50°C, wait until all are dissolved into a solution, add a certain amount of CNTs or GO, stir well, wait until the solution drops to room temperature, add KPS with 0.23 wt%, stir evenly, The solution is sonicated for 20 min, subsequently transferred to the mold, placed in an oven at 70 °C for gelling, and after 30 min, completely gelled, it is removed and placed at 0 °C for 30 min.

2.3. Characterization

2.3.1. Mechanical properties

The mechanical properties of G-A-CNTs hydrogels were obtained by testing with an electric universal testing machine (CMT2103). The tested splines were vegetated by cutting the G-A-CNTs hydrogel into with dimensions of 5 mm in width, 20 mm in length, and 0.2 mm in thickness. The conditions of the test were as follows: at room temperature, a tensile grip was used with a tensile speed of 10 mm/min to generate a stress–strain curve.

2.3.2. Swelling behavior

The swelling rate of G-A-CNTs hydrogel in water is calculated by soaking it in water and measuring its mass change at different times. Considering that its initial mass is R_0 and the mass after soaking for different times and taking out is R_x, then its swelling rate SR can be calculated by Eq. (6):

$$SR = (R_X - R_0)/R_0 \times 100\% \quad (6)$$

2.3.3. Morphology

The microstructure of the G-A-CNTs hydrogel was examined using a Hitachi SU5000 scanning electron microscope (SEM). After freeze-drying the G-A-CNTs hydrogel for 48 h, gold was sprayed on its surface, and the microstructure of the G-A-CNTs hydrogel was observed at 10,000 X and the CNTs in the G-A-CNTs hydrogel was observed at 100,000 X.

2.3.4. Conductivity

The conductivity of G-A-CNTs/G-A-GO hydrogels was measured by a Hall effect test instrument (Ecopia, HMS-5500). The response conductivity of hydrogels with different 0 %-1% CNTs/GO was tested at room temperature without any treatment.

2.3.5. Resistance stability

The resistance stability of the G-A-CNTs hydrogel was tested by the following method: the electronic universal testing machine using UTM5305H was used under the condition of 50 % strain, the tensile frequency was 1 Hz, the periodic load-release cycle, and at the same time, the change of the resistance of the G-A-CNTs hydrogel was

detected by an oscilloscope, and the number of cycles was 2000 times.

2.3.6. Rheological testing

The storage modulus (G') and loss modulus (G'') of the G-A-CNT hydrogel were measured using a rotational rheometer (DHR2, TRIOS, Germany) under frequency changes from 0.1 Hz to 15 Hz at room temperature with a strain of 1.0 %.

2.3.7. XRD

The G-A-CNTs hydrogel was analyzed using an XRD instrument from Rigaku D/Max 2500. The analysis was performed with Cu Kα radiation ($\lambda = 0.154$ nm) at a scan rate of 10°/min, covering a 2θ range of 10° to 90°.

2.4. In vitro cell studies

2.4.1. Isolation and culture of BMSCs

BMSCs were isolated from 3-week-old male SD rats. After euthanasia, hind limbs were disinfected with 75 % ethanol. Femora and tibiae were dissected under sterile conditions, and bone marrow was flushed with DMEM/F-12 (Gibco). The suspension was centrifuged (1000 rpm, 5 min), and the pellet was resuspended in DMEM/F-12 with 10 % FBS (Sigma) and 1 % penicillin–streptomycin (Beyotime). Cells were cultured at 37 °C with 5 % CO_2, with medium replaced daily. Experiments used passages 3–5.

2.4.2. Electrical stimulation

A programmable dual-output DC power supply (CooWey Electronic Industrial Corp., Taiwan) was used for in vitro experiments. Electrode leads were UV-sterilized for 30 min in a biosafety cabinet. In the sterile environment, one terminal was connected to the power supply and the other to cell-laden hydrogels in culture plates, forming a closed circuit. Controlled electrical stimulation (400 mV) was applied daily for 30 min via precise voltage regulation. Six experimental groups were tested: Control, G-A-CNTs 0 %, 0.25 %, 0.5 %, 0.75 %, and 1 %.

2.4.3. Cell biocompatibility

BMSCs were uniformly seeded onto ultraviolet-sterilized hydrogels at a density of 3×10^4 cells/cm^2. Cell proliferation on the hydrogels was assessed at 1, 4, and 7 days following the application of electrical stimulation, using the CCK-8 reagent kit. At the respective time points, the hydrogels were placed in new 12-well plates, with 2 mL of complete medium and 200 μL of CCK-8 reagent was add to the wells. After 1 h of incubation in a cell incubator, 100 μL of sample from each well was carefully pipetted into the corresponding wells of the 96-well plate. And using a microplate reader, the absorbance at 450 nm was measured to evaluate cell proliferation.

To evaluate the cytotoxicity of the scaffolds, a live/dead cell staining assay was performed. The hydrogels were seeded with BMSCs at a concentration of 3×10^4 cells/cm^2. After 4 days of incubation under different conditions, the cells were stained using the Calcein-AM/PI Double Staining Kit (Calcein-AM/PI Live/Dead Cell Staining Kit, Essen Bio, Shanghai, China) and incubated in the dark for 15 min. Cell viability was subsequently assessed using a fluorescence microscope, where live cells emitted green fluorescence and dead cells exhibited red fluorescence.

2.4.4. Evaluation of in vitro osteogenesis

BMSCs (1 × 105 cells/mL) were cultured on scaffolds using Cyagen's OriCell® Rat BMSC Osteogenic Induction Kit (Catalog No. RAXMX-90021, provided by Cyagen Biosciences, China). Medium was changed every 48 h. After 7 and 14 days, ALP and Alizarin Red staining were performed, with excess dye removed by distilled water washing before microscopic evaluation. On day 14, osteogenic differentiation was assessed by RT-qPCR and Western blot for ALP, Runx2, and OCN expression (primer sequences in Table S2; antibody details in Table S3).

2.5. In vivo studies

2.5.1. Animal model construction and hydrogel implantation

In this study, thirty-six male SD rats (approximately 250 g each), acquired from the Animal Centre of Harbin Medical University, were used to establish a model of a critical-sized cranial defect (5 mm in diameter) (Fig. S1b) [42]. All animal procedures adhered to the ethical guidelines set forth in the Declaration of Helsinki and complied with relevant international, national, and institutional protocols governing the humane care and ethical use of animals. The study protocol was granted approval by the Ethics Committee of Harbin Medical University (approval number: YJSDW2024-090). Carbon nanotube hydrogels at varying concentrations were implanted into the defect site and subjected to electrical stimulation, while a hydrogel-only group served as the blank control. The animals were assigned to six groups in a random manner: control, G-A-CNTs 0 %, G-A-CNTs 0.25 %, G-A-CNTs 0.5 %, G-A-CNTs 0.75 %, and G-A-CNTs 1 %. Immediately following surgery, the animals were exposed to electrical stimulation with parameters consistent with those used in previous cellular studies. Treatment was administered daily for 30 min (Fig. S1a).

2.5.2. In vivo biocompatibility assessment

Ten weeks post-surgery, the rats were euthanized, and major organ tissues were collected. The collected tissue samples were preserved in a 4 % paraformaldehyde solution for a period of 48 h, after which they underwent embedding and slicing procedures. Following this, hematoxylin and eosin (H&E) staining was applied to evaluate the G-A-CNT hydrogel's biocompatibility within a living organism.

2.5.3. Micro-CT analysis

The osteogenic effect of the scaffold was evaluated using micro-computed tomography (micro-CT) analysis. Cranial defect samples were scanned with a micro-CT imaging system (Quantum GXII, PerkinElmer, USA). The specimens were positioned in a sample holder and imaged using the following parameters: a scanning resolution of around 14 μm, a full rotation of 360 degrees, a source voltage set at 90 kV, and an applied current of 80 ÀμA. Parametric analyses were conducted using the CT Analyser (CTAn) v.1.18.8.0 (Bruker) to generate 2D images. Adjustments were made using Bruker Software DataViewer v1.7.0.1, while graphical analysis was performed with CTvox v3.3.1.0. A 6 mm diameter circle was selected as the region of interest (ROI), with the internal and external facets of the skull set as the upper and lower limits. The drilling area was then centered and defined. Following this, a 3D reconstruction of the ROI images was conducted. Various bone parameters, such as bone mineral density (BMD) and the ratio of bone volume to total volume (BV/TV), were then quantified to evaluate the three-dimensional architecture of cranial defects and the degree of regeneration.

2.5.4. Histological examination

Staining of the collected hard tissue samples was performed to further investigate the osseointegration of the implanted hydrogel. For histological evaluation, all tissue sections were subjected to both H&E staining and Masson's trichrome staining. Histological images were captured using a standard light microscope. The area of newly formed bone tissue was quantified using ImageJ software to conduct a qualitative analysis of bone formation at 6 and 12 weeks after implantation.

3. Results and discussion

3.1. Preparation of G-A-CNTs/G-A-GO hydrogel

Fig. 1 illustrates the stepwise synthesis procedure for G-A-CNTs and G-A-GO hydrogels. Initially, predetermined amounts of gelatin, acrylamide, and the crosslinker N, N'-methylenebis-acrylamide (MBA) were dissolved in deionized water under constant stirring at 40 °C until the

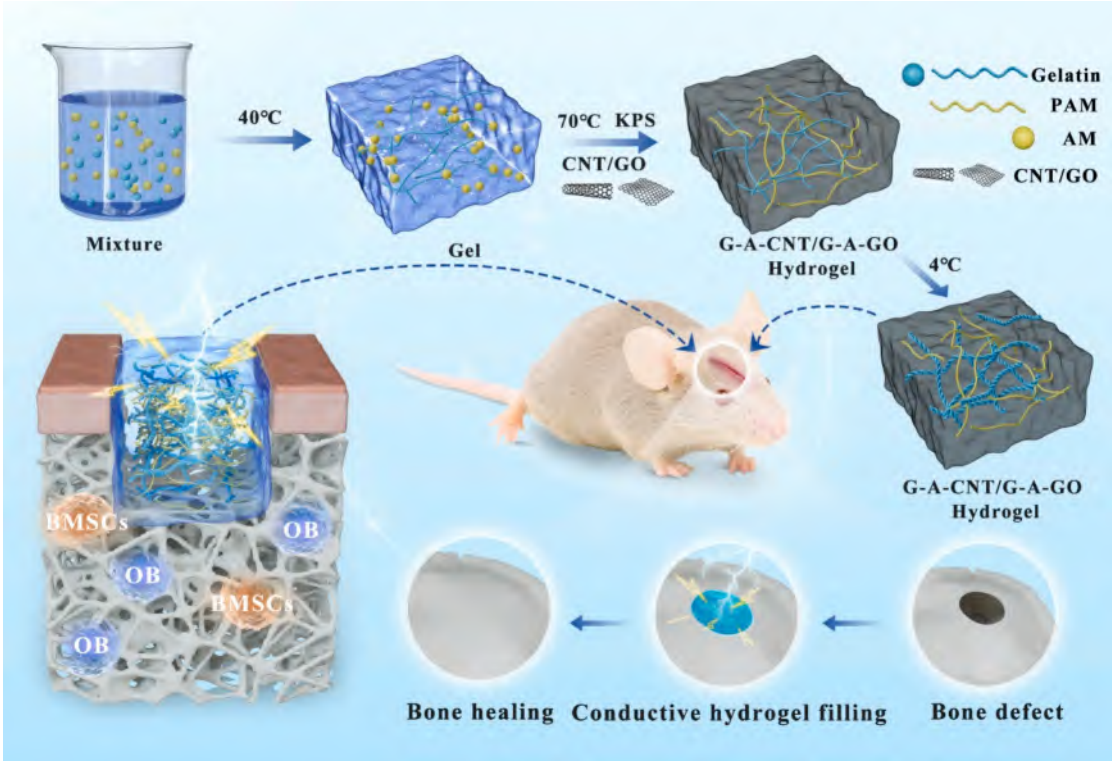

Fig. 1. Electrical stimulation promotes skull repair. Schematic diagram of the preparation of G-A-CNTs/G-A-GO hydrogel, the G-A-CNTs hydrogel was implanted into the skull defect of mice, and the growth of BMSCs and osteoblasts was promoted under the action of electrical stimulation, and then the regeneration and repair of skull tissue were promoted.

gelatin was fully dissolved. Subsequently, CNTs or GO, along with the thermal initiator potassium persulfate (KPS), was incorporated into the mixture. The above obtained solution was stirred thoroughly to ensure homogeneity and then subjected to ultrasonication for 30 min, which facilitated the complete dispersion of CNTs or GO within the solution. The uniform mixture was subsequently transferred into a mold and permitted to solidify at 70 °C for 30 min, after which it was cooled at 4 °C for an additional 30 min, ultimately yielding the G-A-CNTs and G-A-GO hydrogels.The synthesized G-A-CNTs hydrogel was subsequently implanted into the skull defects of mice. Upon the application of electrical stimulation, the hydrogel effectively facilitated the differentiation process of BMSCs as well as osteoblasts, thereby accelerating bone tissue regeneration and promoting efficient skull repair in the mice.

3.2. Conductive of G-A-CNTs/G-A-GO hydrogel

CNTs and graphene are widely regarded as highly effective conductive nanomaterials, extensively utilized in various applications. However, the majority of existing research has focused on studying these materials individually, with comprehensive comparative studies or simultaneous testing largely absent. In this study, the conductivity of G-A-CNTs and G-A-GO hydrogels was systematically investigated through simulation and experimental validation.

Monte Carlo simulations evaluated the conductivity of CNT/graphene/hydrogel composites [43]. The model treated graphene/CNTs as discontinuous conductive phases (CPs) and hydrogel as a continuous non-conductive phase (nCP). While conductivity depends on multiple factors (nanofiller distortion/bending, surface adsorption, hydrogel tunneling), the dominant factor was the conductive network size from CP overlap. The system quantified conductivity through CP contact points, which strongly correlated with composite conductivity.

The simulation process was implemented in Python, with the Flexible Collision Library (FCL) utilized for collision detection and for calculating the number of contact points. The simulation space was defined as a cubic region with dimensions of $5 \times 5 \times 5$ μm^3. Graphene was modeled as a disc with radius r_d and thickness d, while CNTs were represented as cylinders with a cross-sectional radius r_c and length l. For single-layer graphene, the thickness was defined as $d_0 = 1.36nm$.

Each primitive in the simulation space was characterized by two parameters: its spatial position T=(x,y,z), which described its translation, and its pose Ro=(a,b,c,d), which was represented as a quaternion describing its spatial rotation. The corresponding rotation matrix R was expressed as Eq. (1):

$$R = \begin{pmatrix} 1-2c^2-2d^2 & 2bc+2ad & 2bd-2ac \\ 2bc-2ad & 1-2b^2-2d^2 & 2cd+2ab \\ 2bd+2ac & 2cd-2ab & 1-2b^2-2c^2 \end{pmatrix} \quad (1)$$

The spatial transformation of each primitive was then computed as Eq. (2):

$$Transform = R \times T \quad (2)$$

where R is the rotation matrix and T is the translation matrix.

The specific simulation process is as follows: Firstly, CNTs were simulated by randomly generating n CNTs primitives within the simulation space, using a cylindrical model with $r_c = 3$ nm and d = 8 μm. Random spatial transformation matrices T and Ro were generated. The number of contact points for nnn primitives was calculated using the FCL module. As nnn increased, the number of contact points grew, as shown in Fig. 2a for n = 100(i),300(ii),400(iii),4000, 6000, 8000… 52000. The corresponding variation in the contact points for graphene of equivalent mass was also calculated using the following transformation formula (Eq. (3)):

$$n_{graphene} = n_{cnts} \bullet \frac{\left[\pi {r_c}^2 - \pi(r_c - d_0)^2\right] \bullet l}{\pi {r_d}^2 \bullet d} \quad (3)$$

A schematic representation of the graphene simulation is provided in

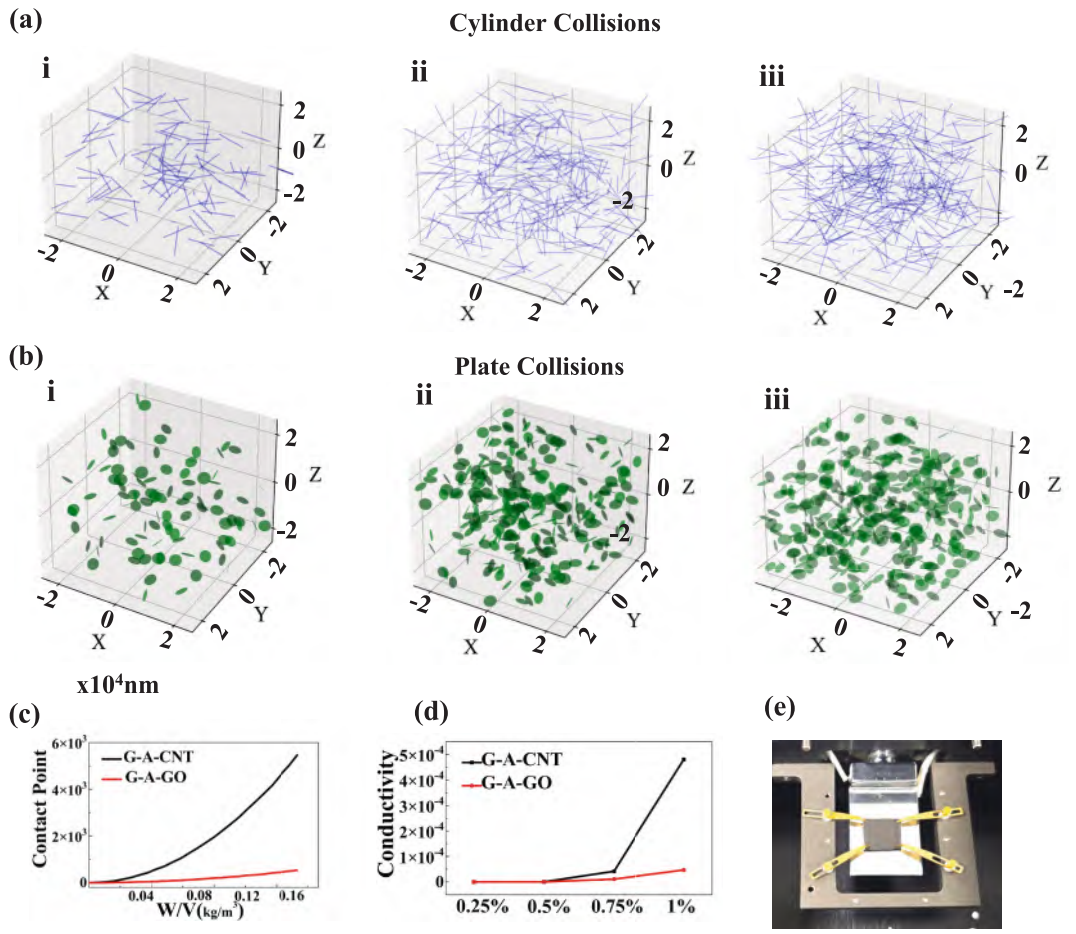

Fig. 2. (a) Schematic representation of CNTs with varying spatial densities in G-A-CNTs conductive hydrogels; (b) Schematic representation of GO with different spatial densities in G-A-CNTs conductive hydrogel; (c) Simulation illustrating the number of collision points within the G-A-CNTs/G-A-GO conductive hydrogel; (d) Results from conductivity tests conducted on the G-A-CNTs/G-A-GO conductive hydrogel (Unit: S/m); (e) Physical depiction of the conductive hydrogel as measured by a Hall effect test instrument.

Fig. 2b. The mass of CNTs and graphene was calculated using the following equations:

For carbon nanotubes, the mass is calculated as Eq. (4):

$$m_c = \left[\pi {r_c}^2 - \pi(r_c - d_0)^2\right] \bullet l \bullet \rho \tag{4}$$

For single-layer graphene, the mass is calculated as Eq. (5):

$$m_d = \pi {r_d}^2 \bullet d \bullet \rho \tag{5}$$

The relationship between the number of CNTs or graphene sheets and their contact points is shown in Fig. 2c. The results revealed that CNTs formed a significantly denser conductive network compared to graphene under identical mass conditions, as evidenced by the faster increase in contact points for CNTs. Furthermore, The quantitative relationship between the number of contacts N and the σ conductivity is derived:

$\sigma = \sigma_0 \times (N - Nc)\hat{}t\ (N > Nc)$.

$\sigma = 0\ (N \leq Nc)$.

When N approaches Nc, the system undergoes a conductor–insulator transition:

- $N < Nc$: Insulating state, $\sigma = 0$.
- $N{=}Nc$: Critical point, $\sigma \propto (N - Nc)t$.
- $N > Nc$: Conducting state, σ continues to increase.

Experimental validation was performed using G-A-CNTs and G-A-GO hydrogels (0.25–1.0 % CNTs/GO). Hall effect measurements (Fig. 2d, e) showed G-A-CNTs' conductivity increased sharply with CNT content, while G-A-GO exhibited a gradual rise. At 0.75 wt%, G-A-CNTs (4.2×10^{-5} S/m) showed ~ 4 × higher conductivity than G-A-GO (1.1×10^{-5} S/m). This difference increased to 10.17-fold at 1.0 wt%, confirming simulations that CNTs form more efficient conductive networks than graphene.

3.3. Effect of KPS on G-A-CNTs hydrogels synthesis

During G-A-CNTs synthesis, KPS concentrations below 0.15 % failed to achieve complete gelation (Fig. S2). While 0.05–0.1 % KPS maintained a liquid state, 0.15 % showed partial gelation and 0.2 % achieved complete gelation. This suggests CNTs may consume sulfate radicals ($SO_4\bullet^-$) through: (1) weak interactions reducing radical-molecule collisions, and (2) charge transfer causing radical quenching, both facilitated by CNTs' conjugated π-bonds.

Ab initio calculations revealed how CNTs affect $SO_4\bullet^-$ activity. Structural optimization and electrostatic potential analysis (Fig. 3a) showed that isolated $SO_4\bullet^-$ has strong nucleophilic regions, whereas $SO_4\bullet^-$ near CNTs loses this feature. Atomic Dipole Moment Corrected Hirshfeld Population (ADCH) charge analysis further confirmed this: isolated $SO_4\bullet^-$ had uneven oxygen charge distribution (−0.55, −0.55, −0.62, −0.09), with one weakly charged oxygen (radical site). In contrast, near CNTs, the charges became uniform (−0.72, −0.72, −0.72, −0.64), indicating radical quenching.

The van der Waals interface analysis (Fig. 3b) revealed penetration between $SO_4\bullet^-$ and CNT surfaces, confirming their interaction.

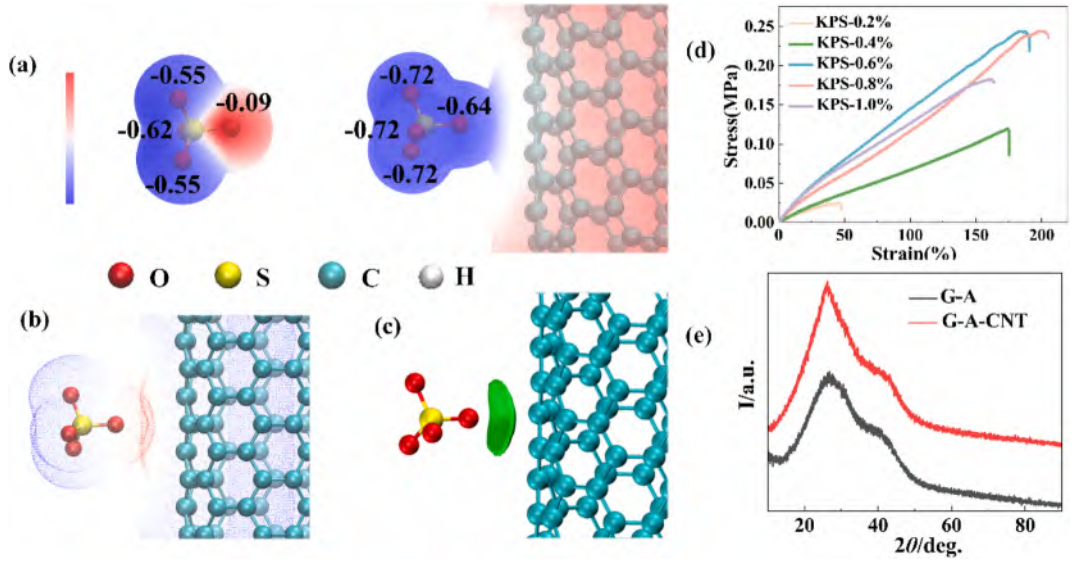

Fig. 3. (a) Schematic representation of the electrostatic potential and ADCH calculation results for sulfate radicals in water and in proximity to CNTs; (b) Calculations of Van der Waals surfaces; (c) IGMH calculations. (d) Mechanical property of G-A-CNT hydrogels with varying KPS contents; (e) XRD analyses of G-A hydrogels and G-A-CNT hydrogels.

Independent Gradient Model based on Hirshfeld Partition (IGMH) analysis (Fig. 3c) quantified this weak interaction (200.74 kJ/mol), indicated by the green interaction zone, demonstrating strong adsorption of $SO_4^{\bullet -}$ onto CNTs. This surface accumulation reduces isolated $SO_4^{\bullet -}$ in solution. Combined with charge transfer effects, CNTs thereby decrease KPS initiation efficiency by both sequestering and

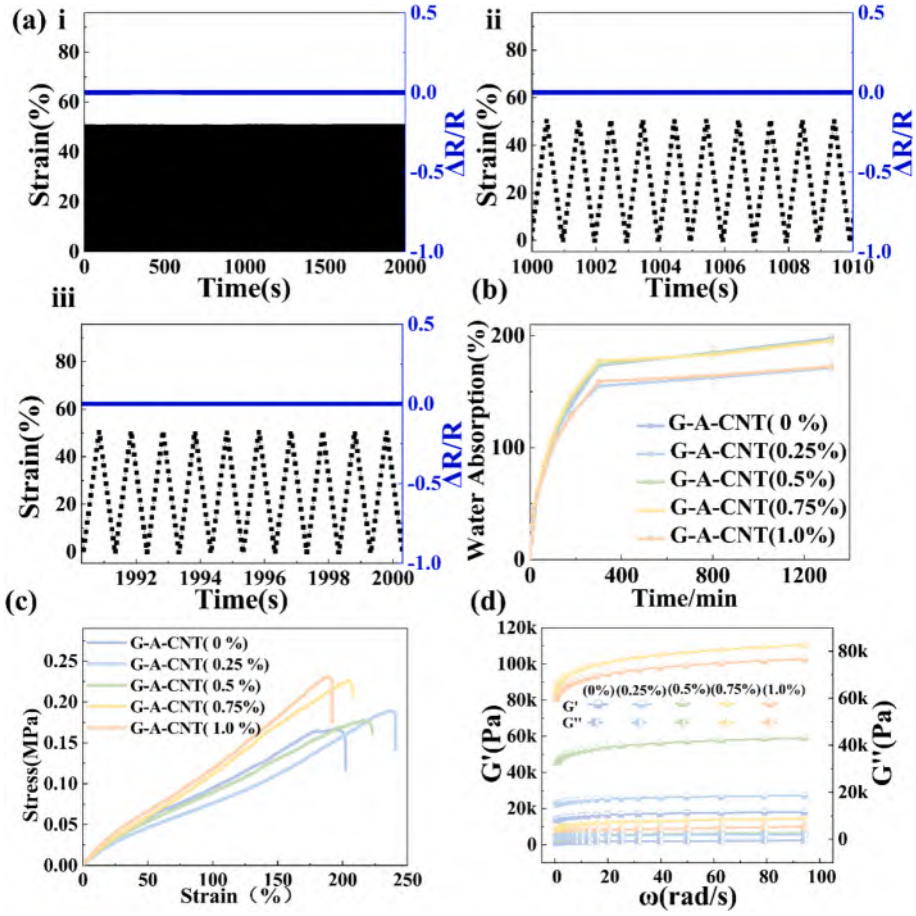

Fig. 4. (a) Conductive cycling stability test of G-A-CNT conductive hydrogel i: 0–2000 times ii 1000–1010 iii 1990–2000 times; (b) Swelling test of G-A-CNT conductive hydrogels with different CNT contents; (c) Mechanical properties test of G-A-CNT conductive hydrogels with different CNT contents; (d) Rheological tests of G-A-CNT conductive hydrogels with different CNT contents.

deactivating $SO_4^{\bullet -}$.

Fig. 3d demonstrates that increasing KPS concentration enhances G-A-CNTs hydrogel mechanical properties, with optimal performance at 0.8 wt% (0.23 MPa tensile strength, 198 % elongation). XRD analysis (Fig. 3e) shows a peak shift confirming CNT-hydrogel integration, while SEM (Fig. S2e, f) reveals a porous structure with well-dispersed CNTs at 10,000 × magnification. These results collectively demonstrate successful CNT incorporation and its role in improving the hydrogel's mechanical and structural properties.

3.4. Performance of G-A-CNTs hydrogels

The conductivity stability of G-A-CNTs hydrogels was evaluated as shown in Fig. 4ai. During the stretching-releasing process, the hydrogel exhibited a reversible and stable relative resistance response. Even after 1000 cycles (Fig. 4ai) and 2000 cycles (Fig. 4aii), the resistance of the hydrogel remained almost unchanged, demonstrating excellent cyclic stability. In addition to conductivity, the hydrogel's swelling characteristics were assessed, as depicted in Fig. 4b. The results indicate that the inclusion of CNTs had minimal impact on the hydrogel's swelling ratio, and the swelling rate stabilized after 7 h. Fig. 4c illustrates that the tensile strength of G-A-CNTs hydrogels increases with CNT content, while toughness exhibits a slight decrease. Specifically, at a CNT concentration of 0.75 wt%, the tensile strength of the G-A-CNT hydrogel was 0.23 MPa, and the elongation at break was 205 %. At a CNT concentration of 1.0 wt%, the tensile strength increased to 0.24 MPa, while the elongation at break decreased to 188 %. The G' and G'' of the G-A-CNTs hydrogels with varying CNTs concentrations were shown in Fig. 4d. The results indicate that both G' and G'' of the hydrogels increased significantly with CNTs content, reaching a peak at a CNTs concentration of 0.75 %. Based on the combined mechanical and rheological properties, the hydrogel achieved optimal performance at a CNTs concentration of 0.75 %.

3.5. Biocompatible of G-A-CNTs hydrogels

We successfully isolated primary BMSCs from rats and cultured them to the third passage. The cells were characterized using flow cytometry, as shown in Fig. 5a. BMSCs were co-cultured with G-A-CNTs hydrogels containing varying concentrations of CNTs for 1, 4, and 7 days. The proliferation of cells within each experimental cohort was meticulously quantified via the CCK-8 assay, as depicted in Fig. 5b. The results showed that cell viability increased with the incubation time in all groups. At various time intervals, data revealed that the incorporation of G-A hydrogels did not markedly influence cellular proliferation when compared to the control group. Conversely, the inclusion of CNTs significantly enhanced cell viability relative to the control, with the most notable augmentation observed in the G-A-CNTs 0.75 % cohort. However, in the G-A-CNTs 1 % group, cell viability was substantially reduced compared to the control, suggesting that hydrogels at this concentration exhibit a degree of cytotoxicity. To further analyze the cytotoxicity of the hydrogels, live/dead staining was performed after 4 days of co-culture. As shown in Fig. 5c, in fluorescence imaging, viable cells emit green fluorescence, while non-viable cells emit red fluorescence. The results revealed that, except for the G-A-CNTs 1 % group, cells on the scaffolds in other groups exhibited good growth, with no significant cell death observed, indicating good cytocompatibility of these scaffolds. In addition, we compared the conductivity and biocompatibility of 0.75 %

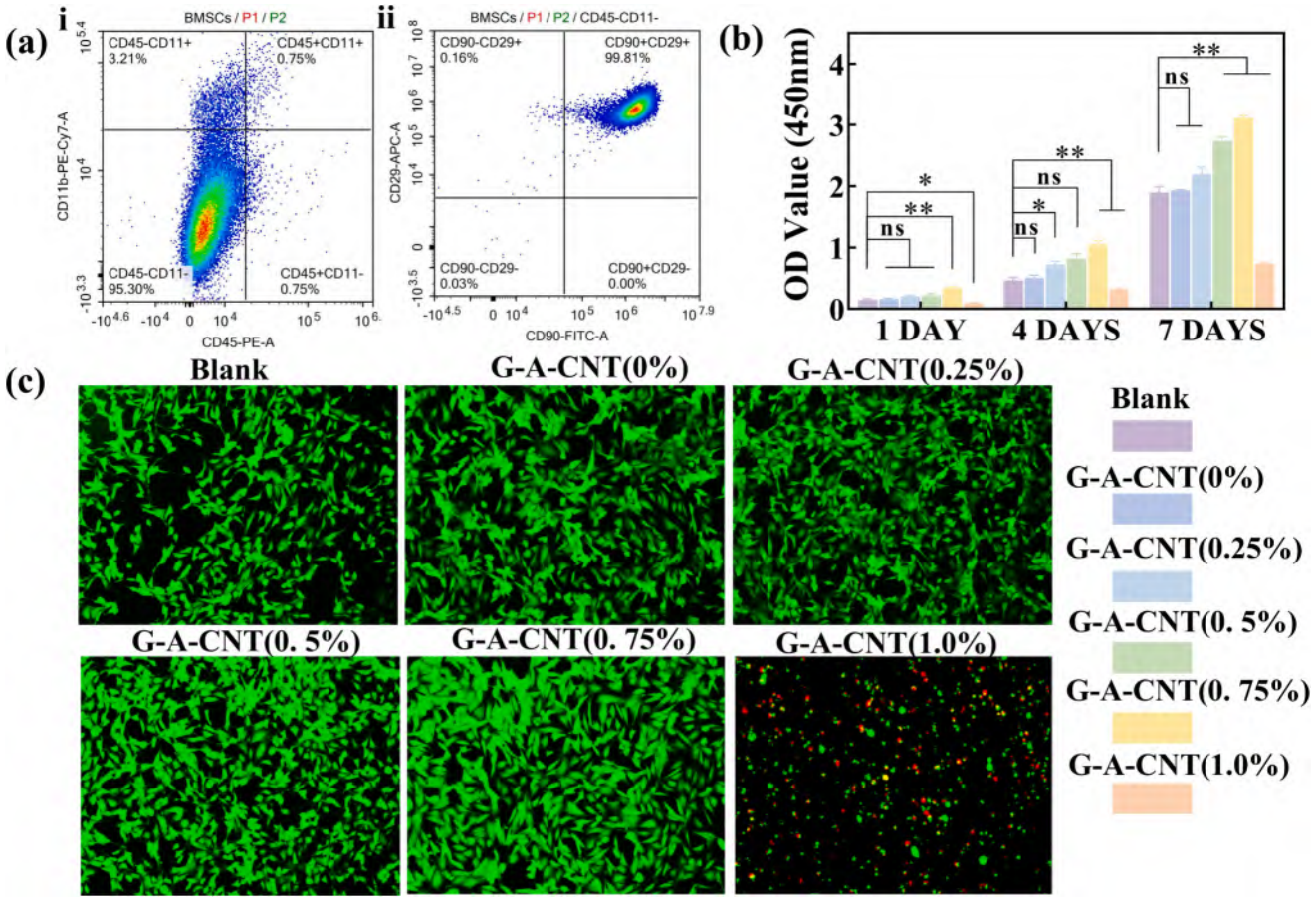

Fig. 5. Results of in vitro cell studies: (a) Results of primary cell identification; (b) CCK-8 assay of cell proliferation in each group; (c) Live/dead cell staining.(*$P < 0.05$, ns $P > 0.05$, **$P < 0.01$).

G-A-CNTs and 0.9 % G-A-CNTs, as shown in Fig. S3. Since the G-A-CNT (0.75 %) formulation already satisfies this requirement while maintaining superior biocompatibility, we have retained it as the optimal composition for our study.

The osteogenic differentiation of BMSCs in vitro was evaluated by assessing ALP activity and calcium nodule deposition. Fig. 6a and 6b present the ALP staining results of BMSCs co-cultured with G-A-CNTs hydrogels for 7 days. No significant difference was detected in the ALP-positive area between the control group and the hydrogel group without CNTs, indicating that the hydrogel alone does not affect cellular differentiation. However, with the incorporation of CNTs, ALP activity increased with the CNTs concentration, with the most substantial improvement observed in the G-A-CNTs group at a concentration of 0.75 %. After 14 days of co-culture under various conditions, osteogenic activity was further validated using Alizarin Red staining (Fig. 6c and 6d). Compared to the control group and the hydrogel without CNTs, the CNTs-doped hydrogels exhibited a greater number of mineralized nodules and stronger osteogenic differentiation. The results of Alizarin Red staining agreed with those of ALP staining, demonstrating that CNTs-doped conductive hydrogels effectively promote osteogenic differentiation. To further evaluate the biocompatibility of the hydrogel, *in vivo* studies were conducted. The H&E staining results of major organ tissues from different rat groups are illustrated in Fig. S4. H&E staining clearly revealed the morphological features and cellular structure of the organs, with no obvious damage or inflammation observed. This indicates that the G-A-CNTs 0 %, G-A-CNTs 0.25 %, G-A-CNTs 0.5 %, and G-A-CNTs 0.75 % hydrogels exhibited good biocompatibility *in vivo*.

To further investigate the effect of different ratios of G-A-A hydrogels on osteogenic performance, we tested the expression of osteogenic genes in hydrogels. RT-qPCR analysis (Fig. 7a-c) further demonstrated that cells cultured on G-A-CNTs 0.75 % hydrogels exhibited significantly higher expression levels of osteogenic genes, including ALP, Runx2, and OCN, compared to other groups. Similarly, Western blot analysis (Fig. 7. b-g) revealed a pronounced upregulation of osteogenic marker proteins in cells co-cultured with G-A-CNTs 0.75 % hydrogels. Taken together, these results highlight the superior osteoinductive potential of G-A-CNTs 0.75 % hydrogels, underscoring their promise as a scaffold for promoting osteogenic differentiation. Fig. 8h elucidates the mechanism of osteogenesis stimulated by electrical impulses. Electrical stimulation enhances the influx of Ca^{2+}, leading to an elevation in intracellular calcium ion concentration. This increase activates multiple signaling pathways, including PI3K/AKT, MAPK, and Wnt/β-catenin, which promote the expression of osteogenesis-related genes. Consequently, this process facilitates the osteogenic differentiation of BMSCs, thereby

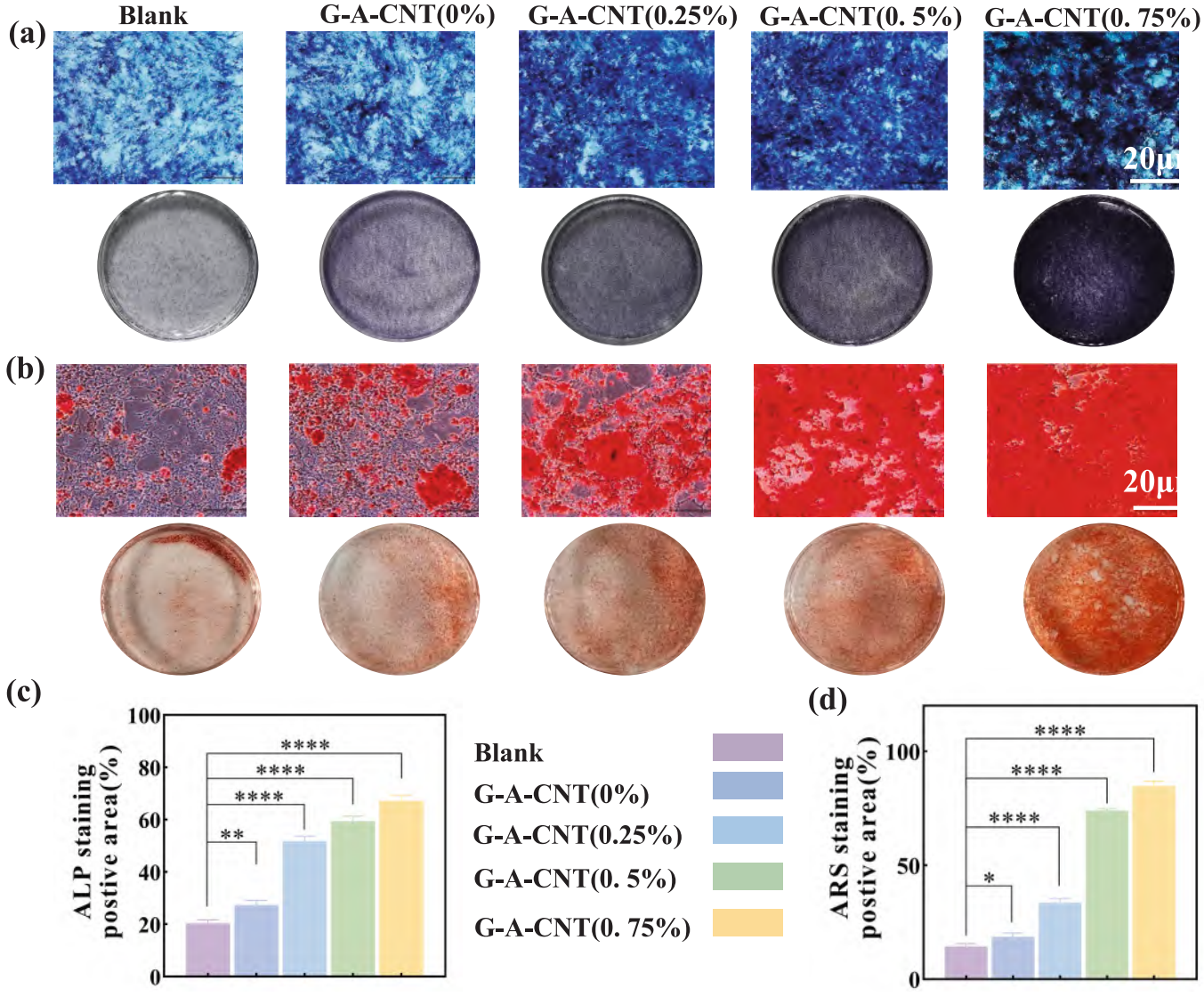

Fig. 6. (a) ALP staining images of BMSCs co-cultured with scaffolds for 7 days; (b) ARS staining images of BMSCs co-cultured with scaffolds for 14 days; (c)Statistical analysis of ALP staining images; (d) Statistical analysis of ARS staining images.(*$P < 0.05$, **$P < 0.01$, ****$P < 0.0001$).

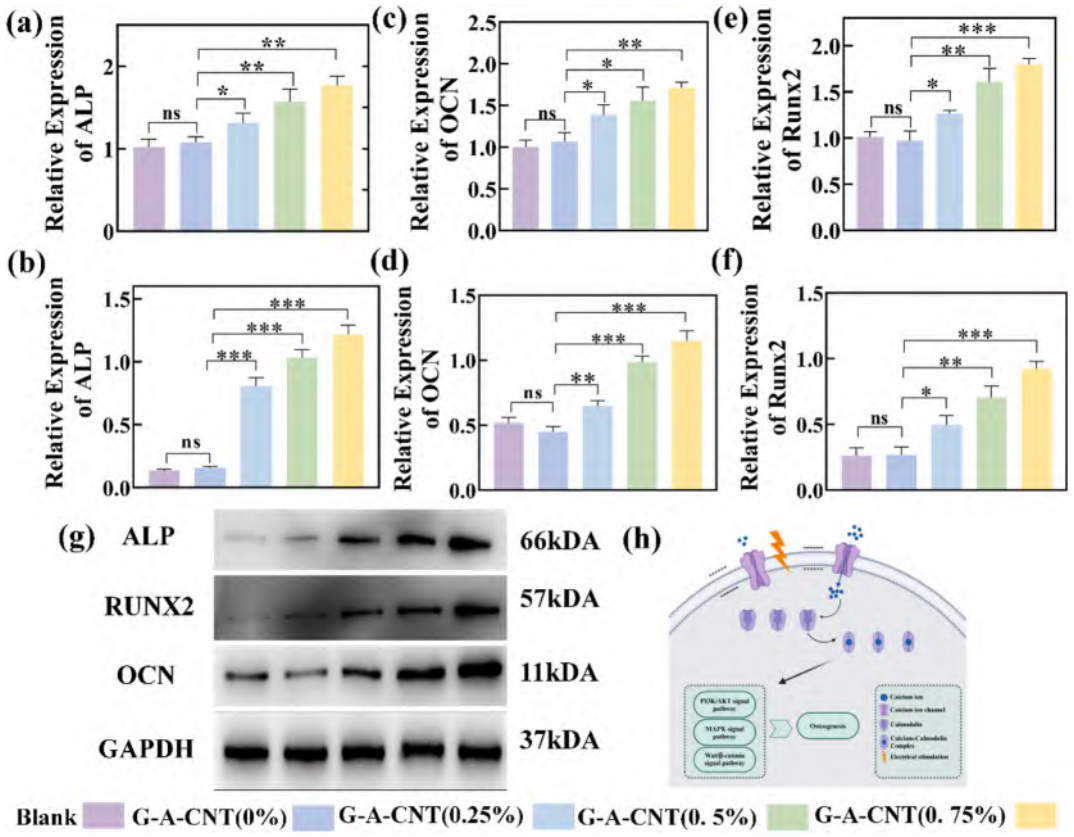

Fig. 7. Expression levels of osteogenesis-related genes and proteins in each group after 14 days of co-culture with hydrogel (a-c)The expression levels of osteogenic genes (ALP, Runx2 and OCN) of BMSCs cultured on different samples on day 14. (b-f)Quantitative analysis of protein band intensities. (g) Western blot assay of ALP, Runx2 and OCN of BMSCs on day 14 (h) The mechanism of bone healing by electrical stimulation.

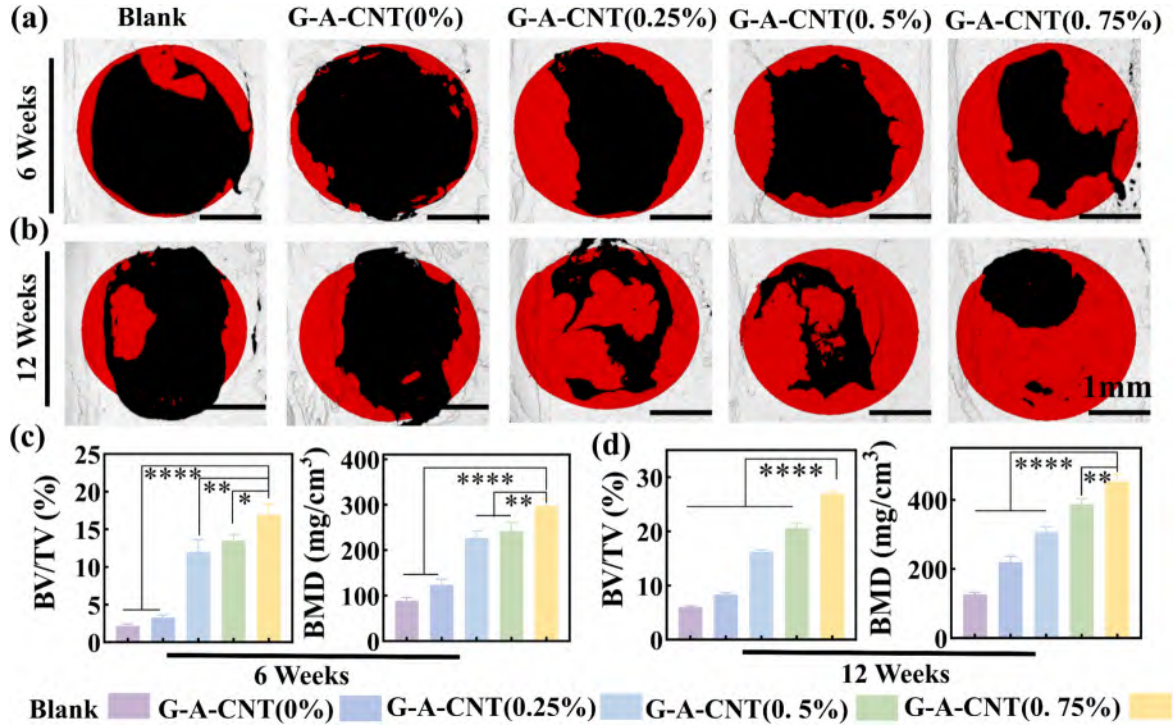

Fig. 8. Results of *in vivo* studies: (a) Top view of micro-CT images of cranial defect sites after 6 weeks and; (b) 12 weeks; (c) Quantitative analysis of bone regeneration parameters at 6 weeks; and (d) 12 weeks. (*$P < 0.05$, **$P < 0.01$, ****$P < 0.0001$).

enhancing osteogenesis.

The fabricated G-A-CNTs hydrogel was surgically positioned into the cranial defect sites of rats. Each experimental group was subjected to a 400 mV voltage stimulation for 30 min daily to investigate its effect on cranial defect repair under microcurrent stimulation. The *in vivo* osteogenic potential of the scaffold was evaluated through radiological and histological analyses. The 3D reconstructions from micro-CT analysis (Fig. 8a) revealed suboptimal bone defect healing in both the untreated and hydrogel-only groups. Even after 12 weeks, only minimal new bone formation was observed at the periphery of the defects, as illustrated in Fig. 8b. In contrast, the 0.75 % G-A-CNTs group demonstrated significantly enhanced bone formation, with new bone almost covering the entire defect. The quantitative assessment of bone formation, based on BV/TV and BMD parameters, provided additional confirmation of these findings (Fig. 8c and 8d). Groups treated with CNTs-doped hydrogels exhibited markedly elevated BV/TV and BMD values relative to the control and hydrogel-only groups. Moreover, these values increased in response to higher CNTs concentrations, reaching their maximum at 0.75 % CNTs. These results indicate that the CNTs-doped conductive hydrogel can effectively promote bone regeneration.

H&E staining (Fig. S5a) revealed no inflammation or pathology in any group. Controls and hydrogel-only groups showed poor defect repair with fibrous tissue, while 0.25 % and 0.5 % G-A-CNTs groups had weak bone bridges with gaps. The 0.75 % G-A-CNTs group demonstrated superior osteogenesis, with nearly continuous bone bridges merging seamlessly with native tissue. Masson staining (Fig. S5b) corroborated these findings: controls and hydrogel groups showed unhealed defects with sparse bone bridges; 0.25 % and 0.5 % groups had partial healing, while the 0.75 % group exhibited robust bone formation-woven bone (blue) and cortical-like lamellar tissue (red) nearly filling the defect. These histological findings were consistent with the results of micro-CT, indicating that the combination of conductive hydrogel and exogenous electrical stimulation significantly promoted bone regeneration.

4. Conclusion

In conclusion, this study developed a conductive G-A-CNT hydrogel with excellent stability and biocompatibility. The incorporation of CNTs enhanced its electrical conductivity and mechanical strength by 44 % compared to the CNT-free hydrogels, supporting bone repair. Under microcurrent stimulation, the G-A-CNT hydrogel significantly boosted cranial regeneration-after 12 weeks, the 0.75 % G-A-CNT group showed near-complete defect coverage. This hydrogel addresses key challenges like material scarcity and infection risks in bone repair, offering promising clinical potential. Future research should explore its efficacy in diverse bone defects and larger animal models.

5. General

Thank others for any contributions, whether it be direct technical help or indirect assistance.

CRediT authorship contribution statement

Qiangwang Geng: Writing – review & editing, Writing – original draft, Methodology, Investigation, Formal analysis, Conceptualization. **Huichao Fu:** Writing – original draft, Methodology, Investigation, Formal analysis, Conceptualization. **Xiongjie Liang:** Investigation. **Xiaoyan Wang:** Investigation. **Yunjiao Wu:** Investigation. **Fenghua Zhang:** Writing – review & editing, Supervision, Conceptualization. **Gongping Xu:** Writing – review & editing, Resources, Conceptualization. **Jinsong Leng:** Writing – review & editing, Resources, Conceptualization.

Declaration of competing interest

The authors declare that they have no known competing financial interests or personal relationships that could have appeared to influence the work reported in this paper.

Acknowledgments

This research did not receive any specific grant from funding agencies in the public, commercial, or not-for-profit sectors.

Appendix A. Supplementary data

Supplementary data to this article can be found online at https://doi.org/10.1016/j.compositesa.2025.109205.

Data availability

The data that support the findings of this study are available from the corresponding author upon reasonable request.

References

[1] Liu C, Ni S, Wu X, Zhang L, Dai T, Wang A, et al. Strontium-modified porous attapulgite composite hydrogel scaffold with advanced angiogenic and osteogenic potential for bone defect repair. Compos Part A Appl Sci Manuf 2024;187:108492. https://doi.org/10.1016/j.compositesa.2024.108492.

[2] Robin M, Mouloungui E, Castillo Dali G, Wang Y, Saffar JL, at.. Mineralized collagen plywood contributes to bone autograft performance. Nature 2024:1–8. https://doi.org/10.1038/s41586-024-08208-z.

[3] Chen X, Yang N, Li B, Gao X, Wang Y, at.. Visualization Analysis of Small Extracellular Vesicles in the Application of Bone-Related Diseases. Cells 2024;13 (11):904. https://doi.org/10.3390/cells13110904.

[4] Xue N, Ding X, Huang R, Jiang R, Huang H, Pan X, et al. Bone Tissue Engineering in the Treatment of Bone Defects. Pharmaceuticals 2022;15:879. https://doi.org/10.3390/ph15070879.

[5] Li Y, Huang L, Tai G, Yan F, Cai L, Xin C, et al. Graphene oxide-loaded magnetic nanoparticles within 3D hydrogel form high-performance scaffolds for bone regeneration and tumour treatment. Compos Part A Appl Sci Manuf 2022;152: 106672. https://doi.org/10.1016/j.compositesa.2021.106672.

[6] Schwartzman JD, McCall M, Ghattas Y, Pugazhendhi AS, Wei F, Ngo C, et al. Multifunctional scaffolds for bone repair following age-related biological decline: Promising prospects for smart biomaterial-driven technologies. Biomaterials 2024; 311:122683. https://doi.org/10.1016/j.biomaterials.2024.122683.

[7] Chen X, Ding M, Yang C, Zhang W, Deng H, Yan D, et al. Fabrication and biological evaluation of poly(amino acid)/bioactive glass/quartz fiber (PAA/BG/QF) composites with potential for bone defect repair. Compos Part A Appl Sci Manuf 2025;190:108697. https://doi.org/10.1016/j.compositesa.2024.108697.

[8] Zhang X, Wang T, Zhang Z, Liu H, Li L, Wang A, et al. Electrical stimulation system based on electroactive biomaterials for bone tissue engineering. Mater Today 2023; 56:68–91. https://doi.org/10.1016/j.mattod.2023.06.011.

[9] Da Silva LP, Kundu SC, Reis RL, Correlo VM. Electric phenomenon: A disregarded tool in tissue engineering and regenerative medicine. Trends Biotechnol 2020;38: 24–49. https://doi.org/10.1016/j.tibtech.2019.07.002.

[10] Zhang W, Li G, Wang B, Zhu Q, Zeng L, Wen Z, et al. Triboelectric nanogenerators for cellular bioelectrical stimulation. Adv Funct Mater 2022;32:2203029. https://doi.org/10.1002/adfm.202203029.

[11] Yao G, Kang L, Li C, Chen S, Wang Q, Yang J, et al. A self-powered implantable and bioresorbable electrostimulation device for biofeedback bone fracture healing. Proc Natl Acad Sci USA 2021;118:e2100772118. https://doi.org/10.1073/pnas.2100772118.

[12] LaGuardia JS, Shariati K, Bedar M. Convergence of calcium channel regulation and mechanotransduction in skeletal regenerative biomaterial design. Adv Healthc Mater 2023;12(27):e2301081. https://doi.org/10.1002/adhm.202301081.

[13] Ma T, Ding Q, Liu C, Wu H. Electromagnetic fields regulate calcium-mediated cell fate of stem cells: osteogenesis, chondrogenesis and apoptosis. Stem Cell Res Ther 2023;14:133. https://doi.org/10.1186/s13287-023-03303-w.

[14] Dagdeviren C, Li Z, Wang ZL. Piezoelectric nano-biomaterials for biomedicine and tissue regeneration. Adv Funct Mater 2020;30:1909045. https://doi.org/10.1002/adfm.201909045.

[15] Wang L, Ma J, Guo T, Zhang F, Dong A, Zhang S, et al. Control of surface wrinkles on shape memory PLA/PPDO micro-nanofibers and their applications in drug release and anti-scarring. Adv Fiber Mater 2023;5:632–49. https://doi.org/10.1007/s42765-022-00249-1.

[16] Cui J, Yu B, Li D, Fu Z, Yang X, Jiang L, et al. Remodeling electrophysiological microenvironment for promoting bone defect repair via electret hybrid electrospun fibrous mat. Adv Fiber Mater 2024;6:1855–73. https://doi.org/10.1007/s42765-024-00457-x.

[17] Zhang Y, He F, Zhang Q, Lu H, Yan S, Shi X. 3D-printed flat-bone-mimetic bioceramic scaffolds for cranial restoration. Res 2023;6:0255. https://doi.org/10.34133/research.0255.
[18] Dutta SD, Ganguly K, Randhawa A, Patil TV, Patel DK, Lim KT. Electrically stimulated 3D bioprinting of gelatin-polypyrrole hydrogel with dynamic semi-IPN network induces osteogenesis via collective signaling and immunopolarization. Biomaterials 2023;294:121999. https://doi.org/10.1016/j.biomaterials.2023.121999.
[19] Chen W, Zhang H, Zhou Q, Zhou F, Zhang Q, Su J. Smart hydrogels for bone reconstruction via modulating the microenvironment. Res 2023;6:0089. https://doi.org/10.34133/research.0089.
[20] Yi D, Lim H, Yim J. Effect of microcurrent stimulation on pain, shoulder function, and grip strength in early post-operative phase after rotator cuff repair. Medicina 2021;57:491. https://doi.org/10.3390/medicina57050491.
[21] Cai K, Jiao Y, Quan Q, Hao Y, Liu J, Wu L, et al. Improved activity of MC3T3-E1 cells by the exciting piezoelectric BaTiO3/TC4 using low-intensity pulsed ultrasound. Bioact Mater 2021;6(11):4073–82. https://doi.org/10.1016/j.bioactmat.2021.04.016.
[22] Chen Y, Chen Y, Xie Z, Yang Y, Chen S, Han T, et al. A biomimetic nanogenerator to enhance bone regeneration by restoring electric microenvironments. ACS Biomater Sci Eng 2024;10:525–36. https://doi.org/10.1021/acsbiomaterials.3c01357.
[23] Kawamura K, Kano Y. Electrical stimulation induces neurite outgrowth in PC12m3 cells via the p38 mitogen-activated protein kinase pathway. Neurosci Lett 2019;698:81–4. https://doi.org/10.1016/j.neulet.2019.01.015.
[24] Luo T, Tan B, Liao J, Shi K, Ning L. A review on external physical stimuli with biomaterials for bone repair. Chem Eng J. 2024:153749. DOI: 10.1016/j.cej.2024.153749.
[25] Konstantinou E, Zagoriti Z, Pyriochou A, Poulas K. Microcurrent stimulation triggers MAPK signaling and TGF-β1 release in fibroblast and osteoblast-like cell lines. Cells 2020;9:1924. https://doi.org/10.3390/cells9091924.
[26] Chen J, Braet F, Brodsky S, Weinstein T, Romanov V, Noiri E, et al. VEGF-induced mobilization of caveolae and increase in permeability of endothelial cells. Am J Physiol Cell Physiol 2002;282:C1053–63. https://doi.org/10.1152/ajpcell.00292.2001.
[27] Song J, Chen Z, Shi L, Yang T, Lu Y, Yu S, et al. A knitted and MXenzyme-integrated dressing for geriatrics diagnosis and ulcer healing. ACS Nano 2024;18:23412–27. https://doi.org/10.1021/acsnano.4c06774.
[28] Xu Q, Dai W, Li P, Li Q, Gao Z, Wu X, et al. Piezoelectric film promotes skin wound healing with enhanced collagen deposition and vessels regeneration via upregulation of PI3K/AKT. Nano Res 2024;17:7461–78. https://doi.org/10.1007/s12274-024-6717-z.
[29] Ma LH, Wang SD, Liu J, Gao H, Zhou W. The design and investigation of hydrogel-based metamaterials with ultra large negative hygroscopic expansion ratio. Int J Smart Nano Mater 2022;13:114–29. https://doi.org/10.1080/19475411.2022.2049393.
[30] Wang X, Yang Y, Luo J, Bai Z. Porous polyurethane hydrogels incorporated with CMC for eliminating methylene blue from water. Int J Smart Nano Mater 2023;14:57–76. https://doi.org/10.1080/19475411.2022.2158958.
[31] Liu Y, Chen Y, Zhu J, Lu M, Jiang C, Fan Z, et al. Time-dependent mechanical behavior of tough hydrogels under multiaxial stretching. Int J Smart Nano Mater 2023;14:460–73. https://doi.org/10.1080/19475411.2023.2255554.
[32] Wu J, Li Y, Duan S, Wang Z, Jing X, Lin Y, et al. Bioinspired stretchable MXene deformation-insensitive hydrogel temperature sensors for plant and skin electronics. Res 2023;6:0106. https://doi.org/10.34133/research.0106.
[33] Shi M, Dong R, Hu J, Guo B. Conductive self-healing biodegradable hydrogel based on hyaluronic acid-grafted-polyaniline as cell recruitment niches and cell delivery carrier for myogenic differentiation and skeletal muscle regeneration. Chem Eng J 2023;457:141110. https://doi.org/10.1016/j.cej.2022.141110.
[34] Zhang Y, Li S, Gao Z, Bi D, Qu N, Huang S, et al. Highly conductive and tough polyacrylamide/sodium alginate hydrogel with uniformly distributed polypyrrole nanospheres for wearable strain sensors. Carbohydr Polym 2023;315:120953. https://doi.org/10.1016/j.carbpol.2023.120953.
[35] Shen K, Liu Z, Xie R, Zhang Y, Yang Y, Zhao X, et al. Nanocomposite conductive hydrogels with robust elasticity and multifunctional responsiveness for flexible sensing and wound monitoring. Mater Horiz 2023;10:2096–108. https://doi.org/10.1039/D3MH00192J.
[36] Arambula-Maldonado R, Liu Y, Xing M, Mequanint K. Bioactive and electrically conductive GelMA-BG-MWCNT nanocomposite hydrogel bone biomaterials. Biomater Adv 2023;157:213616. https://doi.org/10.1016/j.bioadv.2023.213616.
[37] Yu C, Ying X, Shahbazi MA, Yang L, Ma Z, Ye L, et al. A nano-conductive osteogenic hydrogel to locally promote calcium influx for electro-inspired bone defect regeneration. Biomaterials 2023;298:122266. https://doi.org/10.1016/j.biomaterials.2023.122266.
[38] Xie M, Wang Y, Zhang Z, Lin T, Wang Y, Sheng L, et al. Mechanically excellent, notch-insensitive, and highly conductive double-network hydrogel for flexible strain sensor. ACS Appl Mater Interfaces 2024;16(17):22604–13. https://doi.org/10.1021/acsami.4c04310.
[39] Wu M, Liu H, Zhu Y, Chen F, Chen Z, Guo L, et al. Mild photothermal-stimulation based on injectable and photocurable hydrogels orchestrates immunomodulation and osteogenesis for high-performance bone regeneration. Small 2023;19:2300111. https://doi.org/10.1002/smll.202300111.
[40] Zheng W, Xu R, Cao Z, He Y, Chang Y, You Y, et al. Ultrasound-triggered functional hydrogel promotes multistage bone regeneration. Biomaterials 2024;311:122650. https://doi.org/10.1016/j.biomaterials.2024.122650.
[41] Ruggenthaler M, Sidler D, Rubio A. Understanding polaritonic chemistry from ab initio quantum electrodynamics. Chem Rev 2023;123(18):11191–235. https://doi.org/10.1021/acs.chemrev.2c00788.
[42] Chi H, Jiang A, Wang X, Chen G, Song C, Prajapati RK, et al. Dually optimized polycaprolactone/collagen I microfiber scaffolds with stem cell capture and differentiation-inducing abilities promote bone regeneration. J Mater Chem B 2019;7:7052–64. https://doi.org/10.1039/C9TB01359H.
[43] Haghgoo M, Ansari R, Hassanzadeh-Aghdam MK. Monte Carlo analytical-geometrical simulation of piezoresistivity and electrical conductivity of polymeric nanocomposites filled with hybrid carbon nanotubes/graphene nanoplatelets. Compos Part A Appl Sci Manuf 2022;152:106716. https://doi.org/10.1016/j.compositesa.2021.106716.